Narrowband Wavelength Selective Thermal Emitters by Confined Tamm Plasmon Polaritons

Zih-Ying Yang,[†,‡] Satoshi Ishii,*[,‡] Takahiro Yokoyama,[‡] Thang Duy Dao,[‡] Mao-Guo Sun,[§] Pavel S. Pankin,[∥,#] Ivan V. Timofeev,[⊥,#] Tadaaki Nagao,*[,‡,¶] and Kuo-Ping Chen*[,§]

[†]Institute of Lighting and Energy Photonics and [§]Institute of Imaging and Biomedical Photonics, National Chiao Tung University, 301 Gaofa 3rd Road, Tainan 711, Taiwan

[‡]International Center for Materials Nanoarchitectonics (WPI-MANA), National Institute for Materials Science (NIMS), 1-1 Namiki, Tsukuba, Ibaraki 305-0044, Japan

[∥]Institute of Engineering Physics and Radio Electronics and [#]Institute of Nanotechnology, Spectroscopy and Quantum Chemistry, Siberian Federal University, Krasnoyarsk 660041, Russia

[⊥]Kirensky Institute of Physics, Federal Research Center KSC SB RAS, Krasnoyarsk 660036, Russia

[¶]Department of Condensed Matter Physics, Graduate School of Science, Hokkaido University, Kita-10 Nishi-8 Kita-ku, Sapporo 060-0810, Japan

Ⓢ *Supporting Information*

ABSTRACT: This study experimentally demonstrates infrared wavelength selective thermal emission based on Tamm plasmon polaritons (TPPs). Unlike conventional TPP structures, which have a thin metal layer on a distributed Bragg reflector (DBR), the proposed structure has a thick metal under a DBR that is more robust for thermal radiation. The number of DBR pairs is a critical factor in maximizing the narrowband emission needed to satisfy the impedance matching condition, which varies with the choice of metal film. Optimum designs for four different metals, aluminum, gold, molybdenum, and tungsten, are presented. The temporal coupled-mode theory was introduced to explain the origin of the high Q-factor of the proposed structure, which can achieve a twice higher Q-factor for the measured emissivity compared to typical plasmonic thermal emitters. The structure is one-dimensional, consisting of only multilayers and free from nanopatterning, offering a practical design in applications such as gas sensing, narrowband IR sources, and thermophotovoltaics.
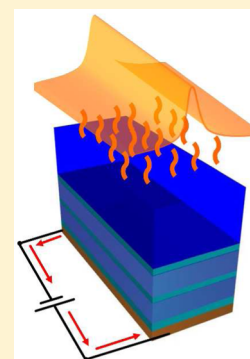
KEYWORDS: *Tamm plasmon polaritons, thermal emission, narrowband absorber*

Wavelength-selective thermal emitters have attracted attention recently owing to the narrowband radiation.[1−3] Choosing specific natural materials that absorb over the required wavelength region can be a way to reduce the unwanted losses, but the absorbing region and the bandwidth are limited by the intrinsic material property without adjustability.[4] In contrast, artificial nanostructures can make a tunable absorber/emitter with a narrow emission peak.[5−7] Different types of nanostructures have been investigated: photonic crystals (PCs) that utilize band edge resonance,[8,9] surface plasmon polaritons (SPPs) resulting from metallic grating structures,[10] gap-plasmon-guided mode of asymmetric T-shaped structures,[11] and magnetic dipole resonance produced by metal−insulator−metal (MIM) metamaterials.[12−16] Regardless of the designs, all the structures listed above require a 2D or 3D nanofabrication process that is costly and hinders practical applications.[17]

To achieve large-area fabrications without added complexity, a planar multilayer structure based on surface-state resonances has many advantages over other 2D or 3D nanostructures. Among multilayer structures, Fabry−Pérot structures have been

demonstrated as wavelength-selective emitters,[18,19] but without stop bands, there would be multiple emission peaks and a low S/N ratio. However, a metallic film combined with a distributed Bragg reflector (DBR) serving as a 1D photonic crystal would be a narrowband emitter with a low background level.[20] In such a structure, Tamm plasmon polaritons (TPPs) with a zero in-plane wavevector have recently garnered increased attention.[21,22] TPP structures are polarization independent, as both TE and TM waves can excite TPPs.[23,24] The tunability of TPPs is readily achieved by changing the stop band of the DBR.[25] TPPs have been researched in theoretical studies on eigenmodes,[26] in combination with metamaterials,[27] in studies on propagating and nonpropagating TPPs,[28] luminescence enhancement,[29] and selective thermal emitters.[30] However, little research has focused on optimizing the absorption and thermal emission peak in the mid-IR region based on TPP structures.

One way to obtain a high quality factor (Q-factor) TPP is by selecting appropriate metallic materials, which has been discussed by Chang et al.[25] In addition, the configuration (see Figure 1) is also an important factor for optimization.
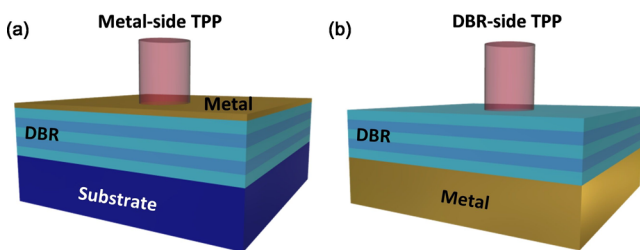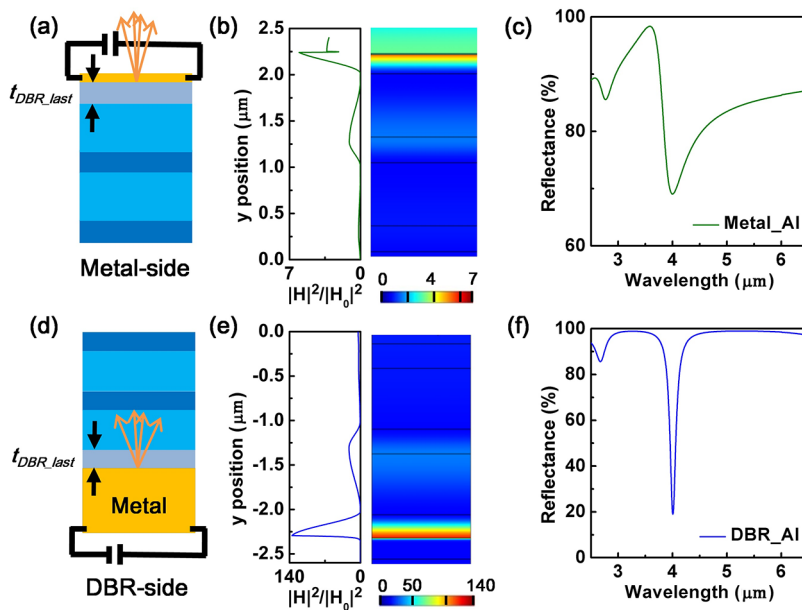

Figure 1. Schematic diagrams of (a) metal-side TPP structure with a thin metal film where light is illuminated from the thin metal layer; (b) DBR-side TPP structure where light is illuminated from the DBR side with an opaque metal film below.

Klimov et al. compared metal-side TPP structures (incident light from the thin metal film) to DBR-side TPP structures (incident light from the DBR) in the visible region.[31] For metal-side TPP structures, metal thickness must be optimized to obtain perfect absorption and a high Q-factor. However, for DBR-side TPP structures, the number of the DBR pairs determines the magnitude of the absorptivity, rather than the metal thickness,[32] so that DBR-side TPP structures can have a thick metal film that behaves as a good reflector with strong evanescent fields excited in the DBR. Moreover, it is understood that DBR-side TPP structures possess better mechanical stability and refractory properties (thick metal film) and decrease fabrication difficulties rising from the fabrication of a continuous ultrathin film.

In this study, DBR-side TPP structures were chosen to demonstrate the ultrasharp emission peak in the mid-IR region. By designing the coupling between localized modes and the incident wave, we analytically and experimentally demonstrate enhanced absorptivity (i.e., emissivity) by DBR-side TPP structures at the designed wavelength. The differences between metal-side TPP structures and DBR-side TPP structures, as well as the design considerations for each structure, are discussed based on coupled mode theory. By taking optical constants and impedance matching into account, optimized conditions of DBR using different metals are presented. The best Q-factor of 36.5 is achieved in experiment by choosing Al as a metal film. The tunability of the DBR-side TPP structures and the emission properties of different metals were experimentally demonstrated, as were the threshold temperature of DBR-side TPP structures using different metals.

In Figure 2, two types of TPP structures having the same 4 μm resonance are compared. Figure 2a shows the metal-side TPP structure with a thin metal film, while the DBR-side TPP structure with an opaque metal film is seen in Figure 2d. As examples, two pairs of DBRs composed of Si and SiO$_2$ layers, combined with an additional Si layer adjacent to an Al film, were chosen to form the TPP structures. As shown in Figures 2b and e, the 2D magnetic field distributions indicate the localized enhancement at the interfaces of the DBR and metal, where the fields exponentially decay into both the metal side and the DBR side. The field enhancement of the DBR-side TPP structure is ~20 times larger than that of the metal-side TPP structure. The simulated reflectances of the metal-side and the DBR-side TPPs aimed at 4 μm are shown in Figure 2c and f. The DBR-side TPP provides a 10 times narrower bandwidth and has greater absorptance compared to the metal-side TPP.

Figure 2. Comparison of the metal-side (Al = 10 nm | Si = 220 nm | 2 pairs DBR aimed at 4 μm) and DBR-side TPP structures (2 pairs DBR aimed at 4 μm | Si = 273 nm | Al = 250 nm). (a, d) Schematic diagrams, (b, e) cross-section plots along the y axis and normalized magnetic field intensity, and (c, f) simulated reflectance spectra for the two TPP structures aimed at 4 μm. In the emission experiment as shown in (a) and (d), current was applied to the metal layer (shown as the circuit with a voltage source) to heat the sample, and the yellow arrows represent the thermal emission from the interface of the DBR/metal due to TPP resonance. The thicknesses of Si and SiO$_2$ were equal to the quarter optical path length of the wavelength equal to 4 μm.
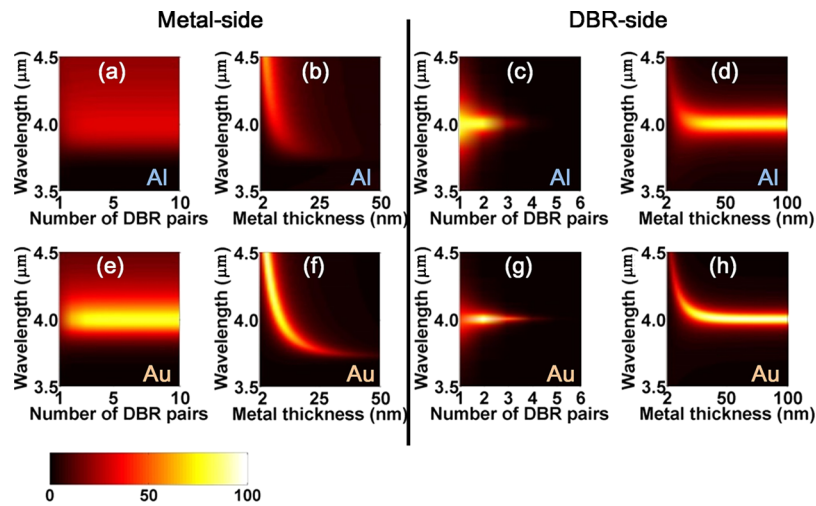
Figure 3. Simulated 2D absorptance maps of the TPP structures. Using Al as the emitting layer for a metal-side TPP design, (a) the number of DBR pairs is varied from 1 pair to 10 pairs and (b) the metal layer thickness was varied from 2 to 50 nm. For a DBR-side TPP design, (c) the number of DBR pairs was varied from 1 pair to 6 pairs and (d) the metal layer thickness was varied from 2 to 100 nm. Using Au as the emitting layer for a metal-side TPP design, (e) the number of DBR pairs was varied from 1 pair to 10 pairs and (f) the metal layer thickness was varied from 2 to 50 nm. For a DBR-side TPP design, (g) the number of DBR pairs was varied from 1 pair to 6 pairs and (h) the metal layer thickness was varied from 2 to 100 nm. The thickness of the Si/SiO$_2$ forming DBR was equal to a quarter of the optical path length of 4 μm, the targeted resonance wavelength. The DBR's last layers were fixed to $t_{\text{DBR\_last}}$ = 220 nm (Al) and 210 nm (Au) for metal-side TPPs and $t_{\text{DBR\_last}}$ = 273 nm (Al) and 265 nm (Au) for DBR-side TPPs, using two pairs of DBR aimed at ~4 μm (λ_{DBR} = 4 μm).
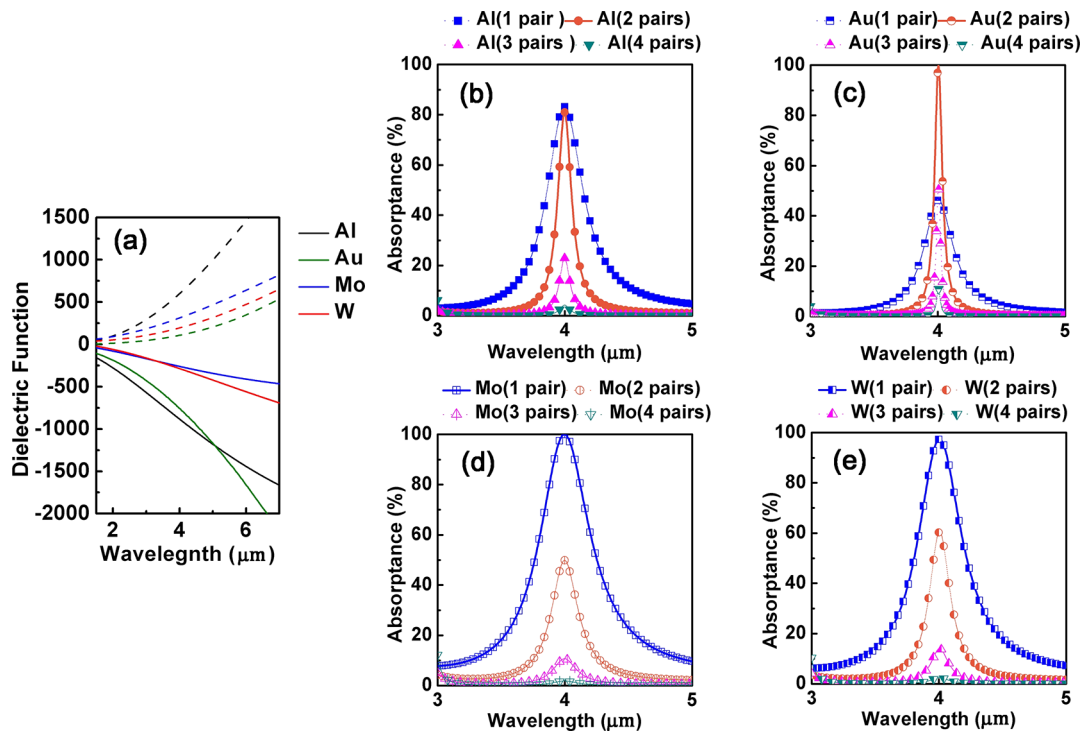
Figure 4. (a) Complex dielectric functions of Al, Au, Mo, and W. The DBR-side TPP structures aimed at 4 μm with the number of the DBR pairs from 1 to 4, using (b) Al, (c) Au, (d) Mo, and (e) W as the emitting metal layer with fixed $t_{\text{DBR\_last}}$ = 273, 265, 263, and 260 nm, respectively.

In order to understand the confined energy in TPPs, the relaxation time (τ) can be used to define the ratio of the stored energy (E) and the leakage power (P),
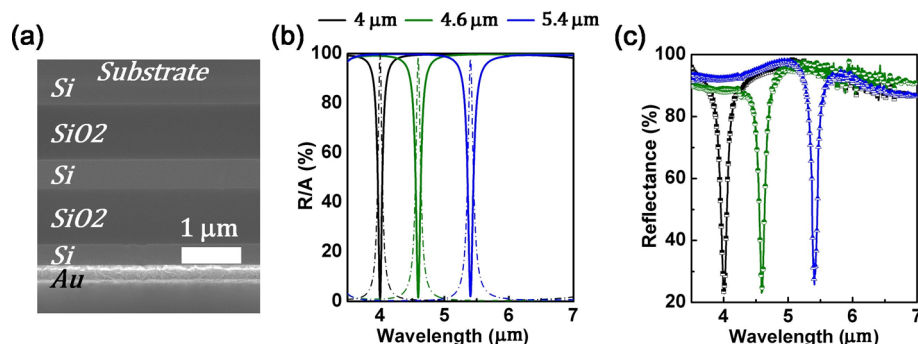
$$\frac{\tau}{2} = \frac{E}{P} \tag{1}$$

The temporal coupled-mode theory can describe the Q-factor of TPP structures by considering the relaxation time,[33,34]

$$\frac{1}{\tau} = \frac{1}{\tau_{\text{DBR}}} + \frac{1}{\tau_{\text{Metal}}} + \frac{1}{\tau_{\text{A}}} \tag{2}$$

$$Q = \frac{\tau \varpi_{\text{TPP}}}{2} \tag{3}$$

where τ_{DBR}, τ_{Metal}, and τ_{A} are the relaxation times due to the transmission loss of the DBR mirror and the transmission and

Figure 5. (a) SEM cross-sectional image of the Au sample with λ_{DBR} = 5 μm (DBR's central wavelength) aimed at 4.6 μm. The thickness for each layer is 392.2 nm (Si), 765.1 nm (SiO$_2$), 392.2 nm (Si), 765 nm (SiO$_2$); t_{DBR_last} = 286 nm (Si), Au = 193.7 nm with Ti = 5 nm as the adhesion layer. (b) Simulated reflectance (solid line) and absorptance (dashed line) spectra and (c) measured reflectance spectra for DBR-side TPP structures with a Si/SiO$_2$ DBR and a 200 nm Au film aimed at 4, 4.6, and 5.4 μm. The DBR-side TPP structures consist of a Si/SiO$_2$ DBR and a 200 nm Au film. (λ_{DBR}, t_{DBR_last}) for emission wavelengths aimed at 4, 4.6, and 5.4 μm are (4 μm, 255 nm), (5 μm, 288 nm), and (5 μm, 387 nm), respectively.

absorption loss of the metals, respectively, and ϖ_{TPP} is the TPP resonance frequency.

Minimization of the three losses is required for better energy storage (larger τ). The critical coupling condition for DBR-side TPPs occurs at larger relaxation times than for metal-side TPPs (see Figure S1 in the Supporting Information). Therefore, a DBR-side TPP structure can support a resonance with a high Q-factor due to lower power leakage.

To investigate the design consideration of the two TPP structures, aluminum (Al) and gold (Au) were chosen as the absorbing/emitting layer in calculating the absorptance spectra maps with various numbers of DBR pairs, as well as various thicknesses of the metal, as shown in Figure 3. When increasing the number of DBR pairs, the absorptance was seen to slightly increase until reaching six pairs of DBRs for metal-side TPP structures (Figure 3a and e). However, there is an optimum number of DBR pairs for DBR-side TPP structures (Figure 3c and g). In terms of the metal film thickness, larger TPP absorptance is realized by decreasing the thickness for a metal-side TPP structure (Figure 3b and 3f), whereas the DBR-side TPP structure demonstrated the opposite (Figure 3d and 3h). Note that when aiming for the mid-IR region, the magnitude of ε' of the metal is much higher than that in the visible/near-IR region, which forces the metal's thickness to be only several nanometers for photon penetration through the metal film, as can be seen in Figure 3b and f. Because of the difficulty in getting smooth and continuous ultrathin metal layers, metal-side TPP structures have disadvantages in fabrication compared to DBR-side TPP structures. For DBR-side TPP structures, an optimized number of DBR pairs, combined with a thick metal layer, is necessary for strong TPP coupling.

As can been seen from Figure 3, the choice of metal is a key factor in TPP resonance. To further investigate how the selection of metals and the number of DBR pairs affects the TPP resonance of DBR-side devices, two plasmonic metals, gold (Au) and aluminum (Al), and two refractory metals, molybdenum (Mo) and tungsten (W), were chosen. The dielectric functions of Al, Au, Mo, and W are shown in Figure 4a. The optical constants of Al, Mo, and W were characterized by spectroscopic ellipsometry (SENDIRA, Sentech). The optical constant of Au was taken from the literature.[35] Figure 4b−e show the simulated absorptance spectra for DBR-side TPP structures aimed at ~4 μm with an increasing number of DBR pairs. When increasing the number of DBR pairs from one to four, the absorptance decreased from ~80% to 4% for Al

samples (Figure 4b), but the Q-factor is the highest when the number of DBR pairs was two. In Figure 4c, for Au samples, the optimized number of DBR pairs was also two. However, different from Al and Au, the absorptance is suppressed as the number of DBR pairs increases from one to four for the Mo and W samples, as can be seen in Figure 4d and e. The reason is that the coupling efficiency of TPP depends on the optical impedance matching (i.e., minimized reflection) at the interface of the DBR and the metal. Since Al and Au have higher reflection coefficients (i.e., larger negative ε') than Mo and W, using Al or Au would support a stronger TPP resonance. In addition, Au or W would provide a narrower bandwidth than Al or Mo, because of the ε'' of Au and W being smaller. Consequently, there are optimized numbers for the DBR pairs when using different metals due to the impedance matching. The metal with larger negative ε' requires DBRs with higher reflectance, leading to a narrower resonance, such as seen in Al and Au. It is worth noting that the metal-side TPP using Au (Figure 3e and f) can support a stronger TPP than using Al (Figure 3a and b), but the performances of the DBR-side structures with Al and Au are comparable (Figure 3c, d, g, and h). This indicates the optical constant of a metal gives more restrictions to the metal-side TPP structures than the DBR-side TPP structures.

For the DBR-side TPP, the critical coupling condition was $\tau_{DBR} = \tau_A$. On the basis of eq 3, the Q-factor is proportional to the relaxation time:

$$Q \propto \tau \propto \tau_A \tag{4}$$

Since the stored energy is the same, the relaxation time has a proportional relationship to the reflectance/transmittance/absorptance as (see temporal-coupled mode theory in the Supporting Information)

$$\tau_{DBR} : \tau_A = \frac{1}{T_{DBR}} : \frac{1}{A_{Metal}} \tag{5}$$

where the T_{DBR} and A_{Metal} are the transmittance of the DBR mirror and absorptance of the metal, respectively.

In addition, at normal incidence, when defining the reflectivity by the refractive index n, and extinction coefficient k, of a metal,[36] the Q-factor for a DBR-side TPP can be simplified as
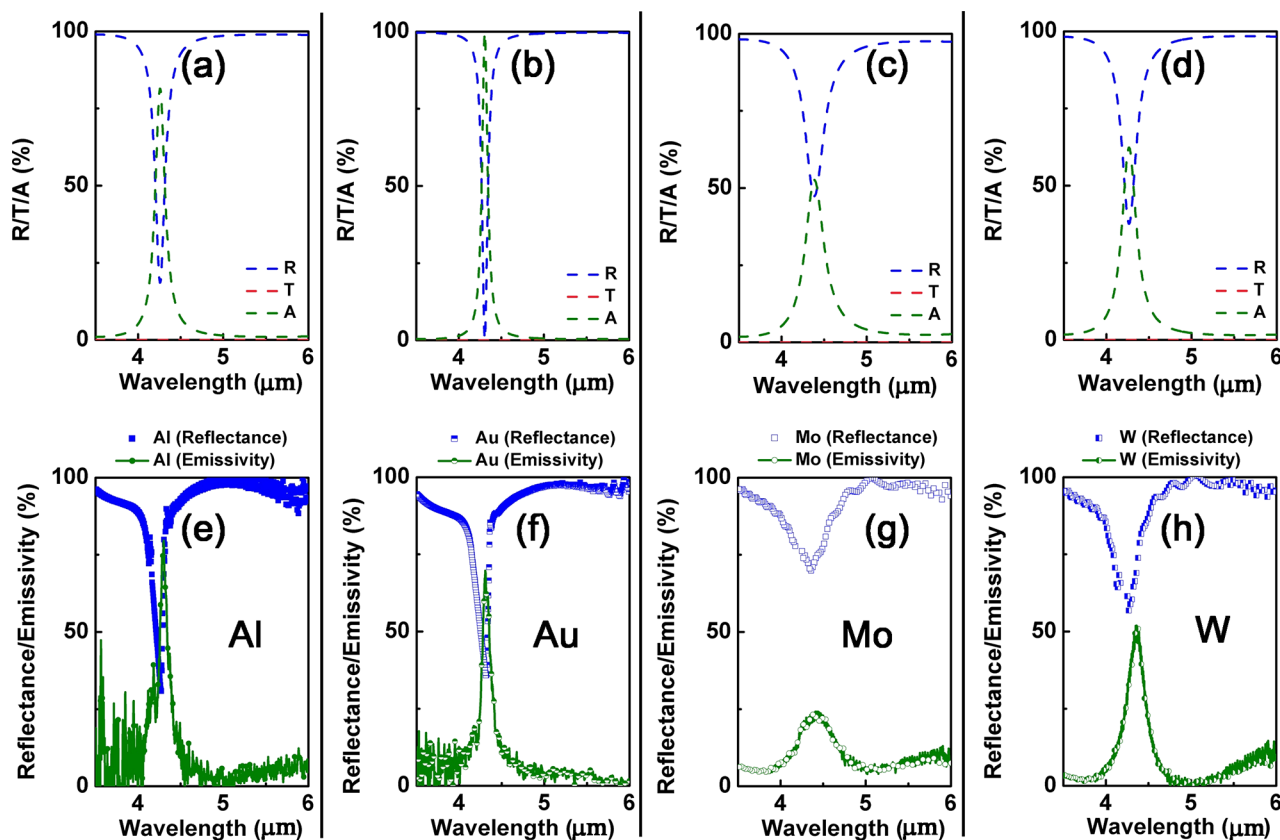
Figure 6. DBR-side TPP emitters aimed at 4.2 μm: simulated reflectance, transmittance, and absorptance spectra using (a) Al, (b) Au, (c) Mo, and (d) W as the emitting layers and the measured reflectance and emissivity for (e) Al, (f) Au, (g) Mo, and (h) W. The t_{DBR_last} for DBR-side TPP emitters using Al, Au, Mo, and W are 295, 292, 300, and 282 nm, respectively. The metal thicknesses are 250 nm for Al, Mo, and W and 200 nm for Au.

$$Q \propto \frac{1}{A_{Metal}} = \frac{1}{1 - R_{Metal}} \propto \frac{k^2}{n} \qquad (6)$$

Thus, considering $n^2 \ll k^2$ for metals, the Q-factor of a DBR-side TPP can be approximated as k^2/n. As shown in Figure 4, the resonance bandwidth of Au is the narrowest and increases for Al, W, and Mo. The trend fits well to k^2/n values of each metal at 4 μm (k^2/n values for Au, Al, W, and Mo are 391, 101, 58, and 39).

EXPERIMENTS AND DISCUSSION

In our experiment, samples aiming at mid-IR were fabricated for Au, Al, Mo, and W. The DBR was composed of Si and SiO$_2$, since it can provide a large photonic band gap that can achieve high reflectance with only two pairs of Si/SiO$_2$.[30] The thickness of the two-pair DBR using Si and SiO$_2$ was equal to the quarter optical path length of the targeted wavelength. First, a two-pair DBR was deposited on a sapphire substrate; then, an additional Si layer was deposited by a magnetron sputtering machine to target each emission wavelength in which the Si layers served as t_{DBR_last}. Afterward, a metal layer of 200 nm was deposited on top of the DBR by an e-gun deposition instrument. Only for Au sample was an adhesive Ti layer of 5 nm deposited before the Au film.

Figure 5a shows the scanning electron miscroscopy (SEM) cross-section image for the 4.6 μm sample with Au. Figure 5b shows the simulated reflectance spectrum (solid line) and simulated absorptance spectrum (dashed line). The simulated spectra were calculated by the transfer-matrix method. An FTIR

spectrometer (iS50R, Thermo Scientific Nicolet) was used for reflectance measurements, with an opaque Au film as a reference. Figure 5c shows the measured reflectance spectra at room temperature. The resonant positions match well to the simulation results. By designing the layer thickness, the tunability of the DBR-side TPP structures was demonstrated in our experiment. Slight discrepancies between the simulation and experimental results might be due to the adhesion layer at the interface.

In the thermal emission measurement, the sample with a thermocouple mounted on the back side was put into an ultra-high-vacuum system (10^{-8} to 10^{-9} Torr) and heated by applying a dc current to the metal layer. The sample sizes were 5×25 mm^2. The emission spectrum of a blackbody paint sample was used as a reference. After heating the sample, the thermal emissions were collected by an FTIR apparatus. Since the bottom metal layer was opaque for DBR-side TPP structures, the impedance matching (i.e., number of DBR pairs) decided how much light reached the interface. In order to study how the metals affected the impedance matching of the DBR-side TPP structures, four different metal layers were tested with the DBR-side TPP structures. Figure 6a−d show the simulated spectra for the Al, Au, Mo, and W samples, respectively. In Figure 6e−h, the measured reflectance and emissivity are shown. The experimental results match well to the simulations with minor discrepancies. The discrepancies might be due to permittivity changes of the metal during the heating and structural imperfections during the thin film deposition (see discrepancy between simulations and experi-

ments in the Supporting Information). The estimated temperatures for the Al and Au samples are ~100 ± 20 and ~400 ± 50 °C for the Mo and W samples during the emission experiments, respectively. In addition, the results of the measured emissivity were also compared to the results in Figure 4. As can be seen in Figure 4a, the ε' values around 4.2 μm are similar between Al and Au and more negative than Mo and W, which results in higher emissivity (and thereby absorptance) for Al and Au samples than for the Mo and W samples.

Further detailed studies were presented for another Al TPP structure aimed at ~4 μm. Figure 7a shows the measured
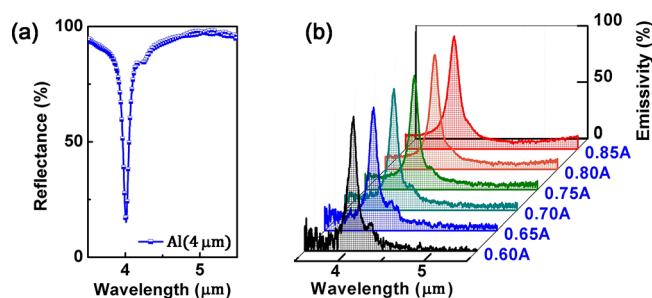
Figure 7. DBR-side TPP structure using Al with two pairs of Si/SiO$_2$ DBRs aimed at 4 μm (t_{DBR_last} = 273 nm, same design as shown in Figure 4b): (a) measured reflectance spectrum at room temperature; (b) emissivity spectra where the heating current varies from 0.6 to 0.85 A.

reflectance, which has a dip value of <0.2, a bandwidth of 110 nm, and a Q-factor of 36.5. In addition, the measured emissivity spectrum using a heating current from 0.6 to 0.85 A (temperature ranging from ~115 to ~270 °C) is shown in Figure 7b. When increasing the heating current, the emissivity peak (λ_{peak}) red-shifted by ~60 nm and the Q-factor slightly decreased from 29.8 to 27.9. When the Q-factor of the Al TPP structure is compared to other metamaterial thermal emitters, it is superior to the Al MIM structure (Q-factor = 14 at 4 μm) by a factor of ~2.0;[17] the Au rectangular-groove structure (Q-factor = 12 at 5.5 μm) by a factor of ~2.3;[37] and the Au cross-shaped MIM structure (Q-factor = 9.2 at 5.8 μm) by a factor of ~3.[13]

Determining the operational temperature range was inevitable in practice.[38,39] To investigate the damage threshold of the TPP structures using different metal materials, the samples were heated by increasing the heating current until the emission peak disappeared or shifted significantly. Table 1 lists the melting temperatures ($T_{melting}$), threshold heating powers (P_{thre}), and threshold heating temperatures (T_{thre}) of the fabricated samples using Al, Au, Mo, and W in the DBR-side TPP structures. Because of their relatively low melting temperatures and threshold heating power, Al and Au samples

Table 1. Melting Temperatures ($T_{melting}$), Threshold Heating Powers (P_{thre}), and Threshold Heating Temperatures (T_{thre}) of DBR-Side TPP Structures Using Al, Au, Mo, and W (Supporting Information, Table S1)

material	$T_{melting}$ (°C)[41]	P_{thre} (mW/mm^2)	T_{thre} (°C)
Al	660	9.0	270
Au	1064	14.5	360
Mo	2623	34.0	750
W	3422	34.6	800

are deemed more suitable for operating temperatures below 300 °C (corresponding to an ideal blackbody's radiation peak, λ_{BB} = 4 to 6 μm), while Mo and W samples could be used for shorter wavelengths, since the sample can be heated to ~800 °C (λ_{BB} = 2.5 to 4 μm) and still retain the emission shape. It can be inferred from Table 1 that the threshold temperature is proportional to the melting temperature. Note that the threshold temperature of a thin film is much lower than the bulk material's melting temperature, as seen in Table 1. The threshold temperature of ~800 °C for a W sample is coincident with the limited stability temperature of W, as reported by Chirumamilla et al.[40] By increasing the temperature to 850 °C, degradation occurred at the W film's interface.

CONCLUSION

We have shown analytically and experimentally that DBR-side TPP structures can demonstrate narrowband selective absorption and thermal emissions in the mid-IR region. Conventionally studied metal-side TPP structures only achieve broad and shallow absorption peaks due to the large $|\varepsilon'|$ of the metal in the mid-IR region. In contrast, a DBR-side TPP structure can mitigate intrinsic properties of the metal, allowing more photons to be coupled to the TPP resonance. By using Al or Au as a metal layer in the DBR-side TPP structures, we obtained a Q-factor that was approximately twice higher than that of other metamaterial-based thermal emitters. Furthermore, besides Au and Al, the refractory metals such as Mo and W may also be used to obtain high emissivity (i.e., absorptivity). The lithography-free feature of the DBR-side TPP structure is more practical compared to other structures having 2D or 3D nanopatterns, making our structure more suitable for use in various mid-IR applications, such as gas sensing, narrowband IR sources, and thermophotovoltaics.

ASSOCIATED CONTENT

S Supporting Information

The Supporting Information is available free of charge on the ACS Publications website at DOI: 10.1021/acsphotonics.7b00408.

TPP structure design; experimental heating conditions; temporal coupled-mode theory; simulated angle characteristics of TPP structures; discrepancy between simulations and experiments (PDF)

AUTHOR INFORMATION

Corresponding Authors
*E-mail: sishii@nims.go.jp.
*E-mail: NAGAO.Tadaaki@nims.go.jp.
*E-mail: kpchen@nctu.edu.tw.

ORCID ⊙
Zih-Ying Yang: 0000-0001-6601-1464
Satoshi Ishii: 0000-0003-0731-8428
Ivan V. Timofeev: 0000-0002-6558-5607
Tadaaki Nagao: 0000-0002-6746-2686

Notes
The authors declare no competing financial interest.

■ REFERENCES

(1) Lenert, A.; Bierman, D. M.; Nam, Y.; Chan, W. R.; Celanović, I.; Soljačić, M.; Wang, E. N. A nanophotonic solar thermophotovoltaic device. *Nat. Nanotechnol.* **2014**, *9*, 126−130.

(2) Greffet, J.-J.; Carminati, R.; Joulain, K.; Mulet, J.-P.; Mainguy, S.; Chen, Y. Coherent emission of light by thermal sources. *Nature* **2002**, *416*, 61−64.

(3) De Zoysa, M.; Asano, T.; Mochizuki, K.; Oskooi, A.; Inoue, T.; Noda, S. Conversion of broadband to narrowband thermal emission through energy recycling. *Nat. Photonics* **2012**, *6*, 535−539.

(4) Torsello, G.; Lomascolo, M.; Licciulli, A.; Diso, D.; Tundo, S.; Mazzer, M. The origin of highly efficient selective emission in rare-earth oxides for thermophotovoltaic applications. *Nat. Mater.* **2004**, *3*, 632−637.

(5) Abbas, M. N.; Cheng, C.-W.; Chang, Y.-C.; Shih, M.-H.; Chen, H.-H.; Lee, S.-C. Angle and polarization independent narrow-band thermal emitter made of metallic disk on SiO2. *Appl. Phys. Lett.* **2011**, *98*, 121116.

(6) Landy, N. I.; Sajuyigbe, S.; Mock, J.; Smith, D.; Padilla, W. Perfect metamaterial absorber. *Phys. Rev. Lett.* **2008**, *100*, 207402.

(7) Inoue, T.; De Zoysa, M.; Asano, T.; Noda, S. Realization of narrowband thermal emission with optical nanostructures. *Optica* **2015**, *2*, 27−35.

(8) Celanovic, I.; Jovanovic, N.; Kassakian, J. Two-dimensional tungsten photonic crystals as selective thermal emitters. *Appl. Phys. Lett.* **2008**, *92*, 193101.

(9) Rinnerbauer, V.; Yeng, Y. X.; Chan, W. R.; Senkevich, J. J.; Joannopoulos, J. D.; Soljačić, M.; Celanovic, I. High-temperature stability and selective thermal emission of polycrystalline tantalum photonic crystals. *Opt. Express* **2013**, *21*, 11482−11491.

(10) Ikeda, K.; Miyazaki, H.; Kasaya, T.; Yamamoto, K.; Inoue, Y.; Fujimura, K.; Kanakugi, T.; Okada, M.; Hatade, K.; Kitagawa, S. Controlled thermal emission of polarized infrared waves from arrayed plasmon nanocavities. *Appl. Phys. Lett.* **2008**, *92*, 1117.

(11) Liao, C. Y.; Wang, C.-M.; Cheng, B. H.; Chen, Y.-H.; Tsai, W.-Y.; Feng, D.-Y.; Yeh, T.-T.; Yen, T.-J.; Tsai, D. P. Quasi-coherent thermal radiation with multiple resonant plasmonic cavities. *Appl. Phys. Lett.* **2016**, *109*, 261101.

(12) Streyer, W.; Feng, K.; Zhong, Y.; Hoffman, A.; Wasserman, D. Selective absorbers and thermal emitters for far-infrared wavelengths. *Appl. Phys. Lett.* **2015**, *107*, 081105.

(13) Liu, X.; Tyler, T.; Starr, T.; Starr, A. F.; Jokerst, N. M.; Padilla, W. J. Taming the blackbody with infrared metamaterials as selective thermal emitters. *Phys. Rev. Lett.* **2011**, *107*, 045901.

(14) Cheng, C.-W.; Abbas, M. N.; Chiu, C.-W.; Lai, K.-T.; Shih, M.-H.; Chang, Y.-C. Wide-angle polarization independent infrared broadband absorbers based on metallic multi-sized disk arrays. *Opt. Express* **2012**, *20*, 10376−10381.

(15) Shemelya, C.; DeMeo, D.; Latham, N. P.; Wu, X.; Bingham, C.; Padilla, W.; Vandervelde, T. E. Stable high temperature metamaterial emitters for thermophotovoltaic applications. *Appl. Phys. Lett.* **2014**, *104*, 201113.

(16) Chen, H.-H.; Hsiao, H.-H.; Chang, H.-C.; Huang, W.-L.; Lee, S.-C. Double wavelength infrared emission by localized surface plasmonic thermal emitter. *Appl. Phys. Lett.* **2014**, *104*, 083114.

(17) Dao, T. D.; Chen, K.; Ishii, S.; Ohi, A.; Nabatame, T.; Kitajima, M.; Nagao, T. Infrared perfect absorbers Fabricated by colloidal mask etching of Al−Al2O3−Al trilayers. *ACS Photonics* **2015**, *2*, 964−970.

(18) Wang, Z.; Luk, T. S.; Tan, Y.; Ji, D.; Zhou, M.; Gan, Q.; Yu, Z. Tunneling-enabled spectrally selective thermal emitter based on flat metallic films. *Appl. Phys. Lett.* **2015**, *106*, 101104.

(19) Wang, L.; Basu, S.; Zhang, Z. Direct measurement of thermal emission from a Fabry−Perot cavity resonator. *J. Heat Transfer* **2012**, *134*, 072701.

(20) Celanovic, I.; Perreault, D.; Kassakian, J. Resonant-cavity enhanced thermal emission. *Phys. Rev. B: Condens. Matter Mater. Phys.* **2005**, *72*, 075127.

(21) Azzini, S.; Lheureux, G.; Symonds, C.; Benoit, J.-M.; Senellart, P.; Lemaitre, A.; Greffet, J.-J.; Blanchard, C.; Sauvan, C.; Bellessa, J. Generation and spatial control of hybrid Tamm plasmon/surface plasmon modes. *ACS Photonics* **2016**, *3*, 1776−1781.

(22) Auguié, B.; Fuertes, M. C.; Angelomé, P. C.; Abdala, N. s. L. p.; Soler Illia, G. J.; Fainstein, A. Tamm plasmon resonance in mesoporous multilayers: toward a sensing application. *ACS Photonics* **2014**, *1*, 775−780.

(23) Vetrov, S.; Bikbaev, R. G.; Rudakova, N.; Chen, K.-P.; Timofeev, I. Optical Tamm states at the interface between a photonic crystal and an epsilon-near-zero nanocomposite. *J. Opt.* **2017**, *19*, 085103.

(24) Huang, S.-G.; Chen, K.-P.; Jeng, S.-C. Phase sensitive sensor on Tamm plasmon devices. *Opt. Mater. Express* **2017**, *7*, 1267−1273.

(25) Chang, C.-Y.; Chen, Y.-H.; Tsai, Y.-L.; Kuo, H.-C.; Chen, K.-P. Tunability and Optimization of Coupling Efficiency in Tamm Plasmon Modes. *IEEE J. Sel. Top. Quantum Electron.* **2015**, *21*, 262−267.

(26) Kaliteevski, M.; Iorsh, I.; Brand, S.; Abram, R.; Chamberlain, J.; Kavokin, A.; Shelykh, I. Tamm plasmon-polaritons: Possible electromagnetic states at the interface of a metal and a dielectric Bragg mirror. *Phys. Rev. B: Condens. Matter Mater. Phys.* **2007**, *76*, 165415.

(27) Lu, H.; Li, Y.; Feng, T.; Wang, S.; Xue, C.; Kang, X.; Du, G.; Jiang, H.; Chen, H. Optical Tamm states in hetero-structures with highly dispersive planar plasmonic metamaterials. *Appl. Phys. Lett.* **2013**, *102*, 111909.

(28) Zhang, X.-L.; Song, J.-F.; Li, X.-B.; Feng, J.; Sun, H.-B. Strongly localized evanescent optical Tamm states at metal-DBR interface. *J. Lightwave Technol.* **2013**, *31*, 1654−1659.

(29) Brückner, R.; Zakhidov, A. A.; Scholz, R.; Sudzius, M.; Hintschich, S.; Fröb, H.; Lyssenko, V.; Leo, K. Phase-locked coherent modes in a patterned metal-organic microcavity. *Nat. Photonics* **2012**, *6*, 322−326.

(30) Yang, Z.-y.; Ishii, S.; Yokoyama, T.; Dao, T. D.; Sun, M.-g.; Nagao, T.; Chen, K.-p. Tamm plasmon selective thermal emitters. *Opt. Lett.* **2016**, *41*, 4453−4456.

(31) Klimov, V. V.; Treshin, I. V.; Shalin, A. S.; Melentiev, P. N.; Kuzin, A. A.; Afanasiev, A. E.; Balykin, V. I. Optical Tamm state and giant asymmetry of light transmission through an array of nanoholes. *Phys. Rev. A: At., Mol., Opt. Phys.* **2015**, *92*, 063842.

(32) Auguié, B.; Bruchhausen, A.; Fainstein, A. Critical coupling to Tamm plasmons. *J. Opt.* **2015**, *17*, 035003.

(33) Fan, S.; Suh, W.; Joannopoulos, J. Temporal coupled-mode theory for the Fano resonance in optical resonators. *J. Opt. Soc. Am. A* **2003**, *20*, 569−572.

(34) Timofeev, I. V.; Pankin, P. S.; Vetrov, S. Y.; Arkhipkin, V. G.; Lee, W.; Zyryanov, V. Y. Chiral optical Tamm states: temporal coupled-mode theory. *Crystals* **2017**, *7*, 113.

(35) Olmon, R. L.; Slovick, B.; Johnson, T. W.; Shelton, D.; Oh, S.-H.; Boreman, G. D.; Raschke, M. B. Optical dielectric function of gold. *Phys. Rev. B: Condens. Matter Mater. Phys.* **2012**, *86*, 235147.

(36) Born, M.; Wolf, E. *Principles of Optics: Electromagnetic Theory of Propagation, Interference and Diffraction of Light*; Elsevier, 1980.

(37) Miyazaki, H.; Ikeda, K.; Kasaya, T.; Yamamoto, K.; Inoue, Y.; Fujimura, K.; Kanakugi, T.; Okada, M.; Hatade, K.; Kitagawa, S. Thermal emission of two-color polarized infrared waves from integrated plasmon cavities. *Appl. Phys. Lett.* **2008**, *92*, 141114.

(38) Yokoyama, T.; Dao, T. D.; Chen, K.; Ishii, S.; Sugavaneshwar, R. P.; Kitajima, M.; Nagao, T. Spectrally selective mid-infrared thermal emission from molybdenum plasmonic metamaterial operated up to 1000° C. *Adv. Opt. Mater.* **2016**, *4*, 1987−1992.

(39) Yang, Z.-Y.; Chen, Y.-H.; Liao, B.-H.; Chen, K.-P. Room temperature fabrication of titanium nitride thin films as plasmonic materials by high-power impulse magnetron sputtering. *Opt. Mater. Express* **2016**, *6*, 540−551.

(40) Chirumamilla, M.; Roberts, A. S.; Ding, F.; Wang, D.; Kristensen, P. K.; Bozhevolnyi, S. I.; Pedersen, K. Multilayer

tungsten-alumina-based broadband light absorbers for high-temperature applications. *Opt. Mater. Express* **2016**, *6*, 2704−2714.

(41) Dean, J. Lange's handbook of chemistry. *Mater. Manuf. Processes* **1990**, *5*, 687−688.